

# A $\delta f$ particle method for gyrokinetic simulations with kinetic electrons and electromagnetic perturbations

Yang Chen and Scott E. Parker

*Center for Integrated Plasma Studies, University of Colorado at Boulder,  
Boulder, CO 80309*

---

## Abstract

A  $\delta f$  particle simulation method is developed for solving the Gyrokinetic-Maxwell system of equations that describes turbulence and anomalous transport in toroidally confined plasmas. A generalized split-weight scheme is used to overcome the constraint on the time step due to fast parallel motion of the electrons. The inaccuracy problem at high plasma  $\beta$  is solved by using the same marker particle distribution as is used for  $\delta f$  to evaluate the  $\beta m_i/m_e A_{\parallel}$  term in Ampere's equation, which is solved iteratively. The algorithm is implemented in three-dimensional toroidal geometry using field-line-following coordinates. Also discussed is the implementation of electron-ion collisional effects which are important when kinetic electron physics is included. Linear benchmarks in toroidal geometry are presented for moderate  $\beta$ , that is,  $\beta \ll 1$ , but  $\beta m_i/m_e \gg 1$ . Nonlinear simulation results with moderate  $\beta$  are also presented.

*Key words:* gyrokinetic simulation;  $\delta f$  method; split-weight scheme; electromagnetic

*PACS*: numbers: 52.65.+z      52.35.Mw

---

## 1 Introduction

Up until recently, gyrokinetic particle simulations of Ion-Temperature-Gradient driven (ITG) microturbulence and turbulence-induced transport typically assumed the electrons to be adiabatic [1–4]. The difficulty of a fully kinetic treatment of electrons in gyrokinetic particle simulations using the  $\delta f$ -method arises from the fact that for typical tokamak plasmas, the electrons move a factor of  $\sim \sqrt{m_i/m_e}$  ( $m_i$  and  $m_e$  are the masses of the ion and the electron) faster than the ions along the magnetic field. This poses a stringent accuracy constraint on the time step that has the form of a Courant condition,  $k_{\parallel} v_{Te} \Delta t \lesssim 1$ .

Various techniques have been employed to overcome this constraint on the time step[5–7]. Among these techniques, the split-weight scheme[7] appears to be especially promising and a generalized version has been implemented for toroidal geometry[8]. Numerical experiments[8] show that for low  $\beta$  cases a time step about one third of that used in typical adiabatic electron simulations can be used for robust nonlinear simulations, whereas  $\delta f$  simulations without the split-weight scheme are numerically unstable for much smaller time steps. However, an accuracy problem due to the use of the split-weight scheme is noticed in the simulation of shear-less slab drift waves, which favors the use of small  $\epsilon_g$ , the split-weight parameter representing the fraction of the total adiabatic electron response proportional to the electrostatic potential[8]. Numerical experiments show that by making a proper choice for  $\epsilon_g$  both accuracy and numerical robustness can be achieved simultaneously.

A more severe problem due to high  $\beta$ , which is previously observed in  $\delta f$  simulations by Cummings[5], is again present in the split-weight scheme[8]. The problem arises from the fact that when the parallel canonical momentum  $p_{\parallel}$  is used as a coordinate, as suggested by Hahm *et. al.* [9], a large current appears in the Ampere's law due to the zero-order distribution [for most applications a Maxwellian distribution in terms of  $p_{\parallel}$ ,  $f_0(p_{\parallel})$ ], which needs to be exactly canceled by the corresponding part carried by the particles and their weights. Any inexact cancellation can potentially lead to a severe accuracy problem. While in slab geometry this difficulty leads to inaccurate results at even moderate  $\beta$  ( $\beta m_i/m_e \geq 1$ ), in toroidal simulations it leads to numerical instability. A similar difficulty is encountered in the so-called continuum method of solving the Gyrokinetic-Maxwell system of equations[10,11], in which an Eulerian grid is used for integrating the gyrokinetic equations. It has been suggested earlier that the resolution of the magnetic skin depth might be necessary to achieve better accuracy[5,10]. However, this is not the case. In particular, recent research indicates that the problem is completely solvable in the continuum approach[11] by judiciously evaluating the current in Ampere's law due to  $f_0(p_{\parallel})$  in a way that is consistent with the evaluation of the current carried by  $\delta f$ . Regarding the particle approach, Lee's recent work suggests that the problem can be solved with a different split-weight scheme[12], pending numerical results from an implementation of the scheme in three dimensions and toroidal geometry.

In this paper we present a solution of the high  $\beta$  problem for the  $\delta f$  particle method, as well as a technique to improve the accuracy of the split-weight scheme. Since electron-ion collisions have been shown to be important for linear physics[13], a Monte-Carlo algorithm for treating the electron-ion collisions when using the  $\delta f$ -method[14] is also described and implemented. The high  $\beta$  problem is solved along the same lines as that used in the continuum approaches, i.e., by evaluating the  $f_{0e}(p_{\parallel})$  contribution to the current in a way that is consistent with the computation of  $\delta f$ . Since in the particle approach,

particle coordinates evolve in time, the matrix resulting from discretizing Ampere's law is dependent on time in a very complicated manner and therefore requires a special technique to invert. We use a hybrid approach which iterates on the particle-coordinates-dependent part of the matrix in Ampere's law, but a direct method to invert the particle-coordinates-independent part of the matrix using Fourier transforms. The algorithm is implemented for an unshifted circular flux surface magnetic equilibrium using the field-line-following coordinates[15]. Extensive linear tests have been performed, including simulations for a shear-less slab geometry, which show good agreement between the code and the linear dispersion relation, in cases where previous algorithms fail [8], and toroidal simulations which agree with Eulerian codes [16,17,11] in terms of both mode frequency and growth rate, for both the finite- $\beta$  stabilization of the ITG mode and the Kinetic Ballooning Mode (KBM).

The paper is organized as follows. In Section II the equations for the Gyrokinetic-Maxwell system of equations is presented in a form ready for particle simulations. Numerical algorithms are described in Section III, with emphasis on the cause of the high  $\beta$  problem and the solution. Examples of simulation, both linear and nonlinear, are presented in Section IV. Concluding remarks are given in Section V.

## 2 $\delta f$ -method for the Gyrokinetic-Maxwell system of equations

### A. Normalization

We consider a toroidal plasma with an on-axis magnetic field strength of  $B_0$ , ion temperature  $T_{0i}$ , electron temperature  $T_{0e}$  and ion number density  $n_0$  at the center of the simulation domain.  $B_0$  is used as unit for measuring magnetic field strength and  $n_0$  for number density. We assume ions are single charged. The ion mass and electron mass are measured in units of the proton mass,  $m_p$ , and are denoted by  $m_i$  and  $m_e$ . Defining  $m_p v_u^2 = T_{0i}$  and  $x_u = \sqrt{m_p T_{0i}}/eB_0$ ,  $v_u$  is used as the unit for velocity,  $x_u$  for the unit length, and time is measured in units of  $t_u = m_p/eB_0$ . Finally, we define  $m_i v_{Ti}^2 = 1$  and  $m_e v_{Te}^2 = T_{0e}/T_{0i} = 1/\tau$ , so that electric potential  $\phi$ , vector potential  $A_\parallel$  and electric current are measured in units of  $T_{0i}/e$ ,  $T_{0i}/ev_u$  and  $en_0v_u$ , respectively.

## B. Equations for split-weight scheme

Using the canonical momentum  $p_{\parallel\alpha} = v_{\parallel\alpha} + \frac{q_\alpha}{m_\alpha} \langle A_{\parallel} \rangle$  as a coordinate, the gyrokinetic equation is written as ( $\alpha = i, e$ )

$$\frac{\partial f_\alpha}{\partial t} + \mathbf{v}_{G\alpha} \cdot \nabla f_\alpha + \dot{p}_{\parallel\alpha} \frac{\partial f_\alpha}{\partial p_{\parallel}} = C(f_\alpha), \quad (1)$$

where

$$\dot{p}_{\parallel\alpha} = \frac{q_\alpha}{m_\alpha} \tilde{\mathbf{b}} \cdot \nabla \langle \phi \rangle - \frac{\mu_\alpha}{m_\alpha} \tilde{\mathbf{b}} \cdot \nabla B + v_{\parallel\alpha} (\mathbf{b} \cdot \nabla \mathbf{b}) \cdot \mathbf{v}_E + \frac{q_\alpha}{m_\alpha} \mathbf{v}_{G\alpha} \cdot \nabla \langle A_{\parallel} \rangle, \quad (2)$$

$\mathbf{v}_{G\alpha} = v_{\parallel\alpha} \tilde{\mathbf{b}} + \mathbf{v}_{d\alpha} + \mathbf{v}_E$  is the guiding center velocity.  $\tilde{\mathbf{b}} = \mathbf{b} + \frac{\langle \delta \mathbf{B}_\perp \rangle}{B}$ ,  $\mathbf{v}_{d\alpha} = \frac{m_\alpha(v_\parallel^2 + v_\perp^2/2)}{q_\alpha B^3} \mathbf{B} \times \nabla B$  is the drift velocity for low  $\beta$  tokamak plasmas with  $\beta \ll 1$ ,  $\mathbf{v}_E = \langle \mathbf{E} \rangle \times \mathbf{b}/B$ . In this paper the electrons are described by the drift-kinetic equations due to their small gyro radii, so  $\langle \phi \rangle = \phi$ , etc., for electrons.  $C(f_\alpha)$  is the collision operator. We do not consider collision effects on ions,  $C(f_i) = 0$ , and use a Lorentzian operator for electrons,  $C(f_e) = C_L(f_e)$ , with

$$C_L(f_e) = \nu_e \frac{1}{2} \frac{\partial}{\partial \lambda} (1 - \lambda^2) \frac{\partial}{\partial \lambda} f_e \quad (3)$$

where  $\lambda = v_{\parallel}/v$  is the pitch angle parameter.  $\nu_e$  is the collision frequency,

$$\nu_e = \frac{n_{0e} e^4 \ln \Lambda}{4\pi \epsilon_0^2 m_e^2 v^3} \left( Z_{\text{eff}} + H_{ee} \left( \sqrt{m_e v^2 / 2T_{0e}} \right) \right) \quad (4)$$

$$\text{with } H_{ee}(x) = \frac{e^{-x^2}}{\sqrt{\pi} x} + (1 - \frac{1}{2x^2}) \text{erf}(x).$$

The ions are simulated using the usual  $\delta f$ -method. Define  $f_i = f_{0i} + \delta f_i$  with  $f_{0\alpha}$  the Maxwellian distribution in  $p_{\parallel\alpha}$  ( $\varepsilon_\alpha = m_\alpha(v_\perp^2 + p_{\parallel\alpha}^2)/2$ ),

$$f_{0\alpha}(\mathbf{x}) = \frac{n_{0\alpha}(\mathbf{x})}{(2\pi)^{3/2} v_{T\alpha}^3(\mathbf{x})} e^{-\varepsilon_\alpha/m_\alpha v_{T\alpha}^2}. \quad (5)$$

$\delta f_i$  evolves according to

$$\frac{d\delta f_i}{dt} = - \left( v_{\parallel i} \frac{\delta \mathbf{B}_\perp}{B} + \mathbf{v}_E \right) \cdot \nabla f_{0i} - \dot{\varepsilon}_i \frac{\partial f_{0i}}{\partial \varepsilon_i} \quad (6)$$

where  $\dot{\varepsilon}_i = \mu_i \mathbf{v}_{Gi} \cdot \nabla B + m_i p_{\parallel i} \dot{p}_{\parallel i}$ .

A fraction of the adiabatic part of the electrons perturbed distribution is treated separately in the split-weight scheme[8]. Thus we write

$$f_e = f_{0e} - \epsilon_g \phi \frac{\partial f_{0e}}{\partial \varepsilon_e} + h. \quad (7)$$

The distribution  $h$  evolves according to

$$\begin{aligned} \frac{dh}{dt} - C_L(f_e) = & - (v_{\parallel e} \frac{\delta \mathbf{B}_\perp}{B} + \mathbf{v}_E) \cdot \nabla f_{0e} - \dot{\varepsilon}_e \frac{\partial f_{0e}}{\partial \varepsilon_e} \\ & + \epsilon_g \left( \frac{\partial \phi}{\partial t} + \mathbf{v}_{Ge} \cdot \nabla \phi \right) \frac{\partial f_{0e}}{\partial \varepsilon_e}. \end{aligned} \quad (8)$$

It is important to keep  $C_L(f_e)$  instead of  $C_L(h)$  in this equation. The collision operator will be discussed further in Section III.

The electric potential  $\phi$  is given by the gyrokinetic Poisson equation[18],

$$(\phi - \tilde{\phi}) + \epsilon_g \tau \phi = \int \delta f_i \delta(\mathbf{R} + \boldsymbol{\rho} - \mathbf{x}) d\mathbf{R} d\mathbf{v} - \int h d\mathbf{v}, \quad (9)$$

where  $d\mathbf{v} = v_\perp dv_\perp dv_\parallel d\xi$ ,  $\xi$  is the gyro angle, and  $\boldsymbol{\rho}$  is the vector leading from a particle's gyrocenter to its actual position.  $\dot{\phi} = \partial \phi / \partial t$  is obtained by taking the time derivative of Eq. 9,

$$\begin{aligned} (\dot{\phi} - \tilde{\phi}) = & \frac{1}{m_e} \nabla_\parallel A_\parallel - \epsilon_g \nabla \cdot \int \phi \frac{\partial f_{0e}}{\partial \varepsilon_e} \mathbf{v}_{Ge} d\mathbf{v} \\ & - \nabla \cdot \int \delta f_i \mathbf{v}_{Gi} \delta(\mathbf{R} + \boldsymbol{\rho} - \mathbf{x}) d\mathbf{R} d\mathbf{v} + \nabla \cdot \int h \mathbf{v}_{Ge} d\mathbf{v} \\ & - \nabla \cdot \left( \int f_{0i} \mathbf{v}_E \delta(\mathbf{R} + \boldsymbol{\rho} - \mathbf{x}) d\mathbf{R} d\mathbf{v} - \int f_{0e} \mathbf{v}_E d\mathbf{v} \right). \end{aligned} \quad (10)$$

In Eq. 9  $\tilde{\phi}$  is defined as

$$\tilde{\phi} = \sum_{\mathbf{k}} \Gamma_0(k_\perp^2 v_{Ti}^2 / \Omega_i^2) \phi_k e^{i\mathbf{k}\cdot\mathbf{x}} \quad (11)$$

with  $\phi = \sum_{\mathbf{k}} \phi_k \exp(i\mathbf{k}\cdot\mathbf{x})$ .  $\dot{\phi}$  and  $\dot{\tilde{\phi}}$  are similarly defined.

The vector potential  $A_\parallel$  is given by Ampere's law,

$$\left( -\nabla_\perp^2 + \frac{\beta_i}{m_e} \right) A_\parallel = \beta_i \left( \int \delta f_i v_\parallel \delta(\mathbf{R} + \boldsymbol{\rho} - \mathbf{x}) d\mathbf{R} d\mathbf{v} - \int h v_\parallel d\mathbf{v} \right). \quad (12)$$

Here  $\beta_i \equiv \mu_0 n_0 T_{0i} / B_0^2$  is related to total plasma  $\beta$  through  $\beta = 2(1 + 1/\tau)\beta_i$ . For typical plasma parameters, the  $\beta_i/m_e$  term on the left-hand-side leads to numerical difficulties[8] and this is the main focus of this paper.

### C. $\delta f$ -method particle simulation

The system of equations Eq. 6 – Eq. 12 are solved using  $\delta f$  particle simulation methods. Thus we define ion and electron weights,  $w_i$  and  $w_e$ , to be proportional to  $\delta f_i$  and  $h$  respectively[1,14]. Particles are typically loaded uniformly in space and Maxwellian in velocity. Weights evolve according to

$$\frac{dw_i}{dt} = -(v_{\parallel i} \frac{\delta \mathbf{B}_{\perp}}{B} + \mathbf{v}_E) \cdot \frac{1}{f_{0i}} \nabla f_{0i} - \dot{\varepsilon}_i \frac{1}{f_{0i}} \frac{\partial f_{0i}}{\partial \varepsilon_i} \quad (13)$$

and

$$\begin{aligned} \frac{dw_e}{dt} = & - (v_{\parallel e} \frac{\delta \mathbf{B}_{\perp}}{B} + \mathbf{v}_E) \cdot \frac{1}{f_{0e}} \nabla f_{0e} - \dot{\varepsilon}_e \frac{1}{f_{0e}} \frac{\partial f_{0e}}{\partial \varepsilon_e} \\ & + \epsilon_g \left( \frac{\partial \phi}{\partial t} + \mathbf{v}_{Ge} \cdot \nabla \phi \right) \frac{1}{f_{0e}} \frac{\partial f_{0e}}{\partial \varepsilon_e}. \end{aligned} \quad (14)$$

The dependence of  $f_{0\alpha}$  on  $\mathbf{x}$  is very weak,  $\rho_i \frac{1}{f_{0\alpha}} |\frac{\partial f_{0\alpha}}{\partial \mathbf{x}}| \ll 1$ , and once the gradients of  $f_{0\alpha}$  are evaluated in the above expressions, the dependence of  $f_{0\alpha}$  on  $\mathbf{x}$  is always dropped, with  $n_{0\alpha}(\mathbf{x})$  and  $v_{T\alpha}(\mathbf{x})$  replaced by 1 and  $v_{T\alpha}$ . The collision operator  $C_L$  is implemented as random pitch-angle scattering in the electron motion equation, as described later. Notice that in the presence of collisions the exact marker distribution along the (random) particle trajectories cannot be known[14] and is approximated by  $f_{0e}$  in the electron weight equation. The crucial nonlinear  $\mathbf{E} \times \mathbf{B}$  dynamics and the perturbed motion due to magnetic fluttering,  $v_{\parallel} \delta \mathbf{B}/B_0$ , are included in the guiding center velocity  $\mathbf{v}_{G\alpha}$ .

## 3 Algorithm

A Predictor-Corrector scheme is used for evolving particle coordinates and the weight equations. Gyro-averaging is done with the four-point averaging procedure[19]. Field solvers and the collision operator are described below.

### A. Solving Ampere's law

The  $\beta_i/m_e$  term in Ampere's law, Eq. 12, and the first term on the right hand side (RHS) of Eq. 10 represent contributions of the electric current carried by  $f_{0e}(p_{\parallel})$ , i.e.,

$$\delta j[f_{0e}] = \frac{1}{m_e} \int f_{0e}(v_{\perp}, p_{\parallel}) A_{\parallel}(\mathbf{x}) d\mathbf{v} = \frac{1}{m_e} A_{\parallel}. \quad (15)$$

The corresponding ion term is small compared with the electron term and is therefore neglected. Due to the large mass ratio  $\beta_i/m_e$  is typically much larger than  $k_\perp^2 \rho_i^2$ . This term has to be largely canceled by part of  $\int h v_{\parallel} d\mathbf{v}$ . This can be easily seen by noticing the fact that in a uniform plasma the Alfvén mode frequency is independent of the mass ratio at moderate  $\beta$ , consequently, the explicit strong dependence on the mass ratio in Eq. 12 should be canceled out. However, with discrete particle effects and finite particle shape effects involved in the evaluation of the  $\beta_i \int h v_{\parallel} d\mathbf{v}$  term, inexact cancellation occurs. This difficulty arises because we have chosen  $f_{0\alpha}$  in the  $\delta f$  scheme to be Maxwellian in terms of the canonical momentum (to eliminate  $\partial A_{\parallel}/\partial t$  from the equations), instead of Maxwellian in terms of  $v_{\parallel}$ . The difference between the two,  $f_{0e}(v_{\parallel}) - f_{0e}(p_{\parallel})$ , is represented in particle weights. In particle simulations the current carried by particles is computed by summing over the product of individual particle velocity and weight, therefore is explicitly dependent on particle velocities. Our approach to facilitate the cancellation between the two currents, that comes from  $f_{0e}$  and that comes from  $f_{0e}(v_{\parallel}) - f_{0e}(p_{\parallel})$ , is to rewrite  $\delta j[f_{0e}]$  in a form that shows explicit velocity dependence and, subsequently, to replace  $f_{0e}$  by its discrete representation. We first rewrite Eq. 15 as

$$\delta j[f_{0e}] = \tau \int f_{0e}(v_{\perp}, p_{\parallel}) p_{\parallel}^2 A_{\parallel}(\mathbf{x}) d\mathbf{v}. \quad (16)$$

No approximation is made here, however, Eq. 16 allows better cancellation between the two currents when the velocity integral is replaced by summing over particles. This can be seen by examining the linear part of  $f_{0e}(v_{\parallel}) - f_{0e}(p_{\parallel})$ ,

$$f_{0e}(v_{\parallel}) - f_{0e}(p_{\parallel}) \approx -\tau p_{\parallel} A_{\parallel} f_{0e}(p_{\parallel}), \quad (17)$$

which is part of the particle weight. The current from this linear part is the same as that coming from  $f_{0e}(p_{\parallel})$  but in the opposite direction,

$$\int (-\tau p_{\parallel} A_{\parallel} f_{0e}(p_{\parallel})) v_{\parallel} d\mathbf{v} = -\frac{1}{m_e} A_{\parallel}. \quad (18)$$

When computing the perturbed electric current from the particle weights the integral in this equation is of course replaced by summing over particles. The point here is that, when the difference between  $v_{\parallel}$  and  $p_{\parallel}$  in the integrand of Eq. 18 is neglected, the integrals in Eq. 16 and Eq. 18 have the same velocity dependence.

We next replace  $f_{0e}$  in Eq. 16 with its discrete representation (with proper normalization),

$$\tilde{f}_{0e} \approx \frac{V}{N} \frac{1}{2\pi v_{\perp}} \sum_j \delta(\mathbf{x} - \mathbf{x}_j) \delta(v_{\perp} - v_{\perp j}) \delta(v_{\parallel} - v_{\parallel j}), \quad (19)$$

here  $V$  is the volume of the simulation domain and  $N$  total number of electrons

used in the simulation. The tilde notation stands for the numerical representation.

In addition to using the same set of discrete particles, the same scattering operation as that used for  $\int h v_{\parallel} dv$  has to be used to distribute  $A_{\parallel}$  at the particle location to nearby grid points. That is,

$$\tilde{\delta j}[f_{0e}](\mathbf{x}) \approx \frac{V}{N} \tau \sum_j p_{\parallel j}^2 A_{\parallel}(\mathbf{x}_j) S(\mathbf{x} - \mathbf{x}_j). \quad (20)$$

Here  $S(\mathbf{x})$  is the particle shape function used to deposit the particle current to nearby grid points. A triangular shape is typically used in each dimension. Thus  $S(\mathbf{x}) = S_{1D}(x/\Delta x)S_{1D}(y/\Delta y)S_{1D}(z/\Delta z)$  ( $\Delta x$ ,  $\Delta y$  and  $\Delta z$  are the grid sizes) with

$$S_{1D}(x) = \begin{cases} 1 - |x| & \text{for } |x| \leq 1 \\ 0 & \text{for } |x| > 1. \end{cases} \quad (21)$$

The value of  $A_{\parallel}$  at the particle location  $\mathbf{x}_j$  in Eq. 20 is calculated from the values at the neighboring grids using the same shape function,

$$A_{\parallel}(\mathbf{x}_j) = \sum_{l,m,n} A_{\parallel}(\mathbf{x}_{l,m,n}) S(\mathbf{x}_j - \mathbf{x}_{l,m,n}), \quad (22)$$

where  $\mathbf{x}_{l,m,n}$  is the location of the grid indexed  $(l, m, n)$ . When we replace the  $\beta_i/m_e$  term in Eq. 12 with  $\tilde{\delta f}[f_{0e}]$  in Eq. 20, the resulting equation for  $A_{\parallel}$ , upon discretization, has a matrix that involves particle coordinates. It is solved iteratively. We rewrite Ampere's law as

$$\left( -\nabla_{\perp}^2 + \frac{\beta_i}{m_e} \right) A_{\parallel}^{n+1} = \beta_i (\tilde{\delta u}_{\parallel i} - \tilde{\delta u}_{\parallel e}) + \beta_i \left( \frac{1}{m_e} A_{\parallel}^n - \tilde{\delta j}[f_{0e}] \right), \quad (23)$$

where  $\tilde{\delta u}_{\parallel i}$  and  $\tilde{\delta u}_{\parallel e}$  result from numerically evaluating the corresponding terms in Eq. 12. The superscript  $n$  stands for current values, and  $A_{\parallel}^n$  is used in the evaluation of  $\tilde{\delta j}[f_{0e}]$  according to Eq. 20. Given the form of the RHS of Eq. 23,  $A_{\parallel}^{n+1}$  is solved using Fourier transforms[8]. Typically, 5 – 7 iterations are needed to ensure convergence.

Numerical experiments show that for shear-less slab simulations, rewriting of  $\tilde{\delta j}[f_{0e}]$  in the form of Eq. 16 is not necessary. In other words the factor  $p_{\parallel j}^2/m_e$  in Eq. 20 can be ignored in the shear-less slab limit. This is because in a shear-less slab geometry particle motion is extremely simple, with Maxwellian loading in velocity and uniform loading in space the marker density in principle remains so (at least linearly) in the simulation and dropping the velocity dependence in Eq. 20 causes no systematic change. The finite particle size effects in Eq. 20,  $S(\mathbf{x} - \mathbf{x}_j)$ , leads to a systematic difference between  $\tilde{\delta j}[f_{0e}]$

and  $\delta j[f_{0e}]$  that cannot be eliminated by merely increasing the number of particles. In toroidal simulations there could be a small but systematic difference between the marker density and a local Maxwellian distribution due to effects such as particle drifts, boundary conditions and nonuniform resolution of the simulation domain due to the use of the field-line-following coordinates, and we find that rewriting Eq. 15 in the form of Eq. 16 is important.

### B. The computation of $\phi$ and $\dot{\phi}$

The quasi-neutrality condition, Eq. 9, is solved spectrally as described previously[8]. Eq. 10 is solved with the following modification: Consistent with replacing  $\delta j[f_{0e}]$  with  $\tilde{\delta j}[f_{0e}]$  in Ampere's law,  $\tilde{\delta j}[f_{0e}]$  is also used for evaluating the first term on the RHS of Eq. 10. The second term on the RHS of Eq. 10 is evaluated as previously described[8]. The integrals in the third term and the fourth term are evaluated by depositing particle's weighted velocity,  $w_j \mathbf{v}_{G0j}$ , to the grid points. Only the unperturbed guiding center velocity  $\mathbf{v}_{G0}$  is used here. In general only linear terms on the RHS of Eq. 10 and Eq. 12 are retained.

The last term in Eq. 10 represents the rate of change of charge density due to  $\mathbf{E} \times \mathbf{B}$  convection of  $f_{0\alpha}$ . Due to finite ion Larmor radius effects it is not negligible. In our previous implementation of the split-weight scheme this term was evaluated using a Fourier representation for  $\phi$ , with gyro-averaging and the integration over  $f_{0\alpha}$  performed analytically[8]. We have found that this is again inconsistent with the discrete particles used to evaluate the charge density in Eq. 9 and the four-point scheme for gyro-averaging. It is easy to see that numerically this term comes from the  $\mathbf{v}_E \cdot \nabla f_{0\alpha}$  terms in the weight equations, Eq. 13 and Eq. 14. More specifically, we evaluate this part of the rate of change of the charge density due to  $f_{0\alpha}$ ,  $\frac{\partial \rho_q}{\partial t} \Big|_{f_0}$ , according to

$$\begin{aligned} \frac{\partial \rho_q}{\partial t} \Big|_{f_0} = & - \sum_{i's} \frac{1}{4} \sum_{l=1}^4 \left( v_E \cdot \frac{1}{f_i} \nabla f_{0i} \right)_j S(\mathbf{x}_j + \boldsymbol{\rho}_l - \mathbf{x}) \\ & + \sum_{e's} \left( v_E \cdot \frac{1}{f_{0e}} \nabla f_{0e} \right)_j S(\mathbf{x}_j - \mathbf{x}), \end{aligned} \quad (24)$$

here four equally-spaced points along the ion gyro-orbits, indexed by  $l$ , are chosen, and  $\boldsymbol{\rho}_l$  is the vector leading from the gyrocenter  $\mathbf{x}_j$  to the point  $l$ . Consistent with the gyro-averaging in particle pushing,  $\mathbf{v}_E$  for ions in Eq. 24 is also evaluated using a four-point averaging not explicitly written in Eq. 24.

### C. The Lorentz operator

Using Eq. 7 we have

$$C_L(f_e) = C_L(f_{0e}(p_{\parallel})) - C_L(\epsilon_g \phi \frac{\partial f_{0e}}{\partial \varepsilon_e}) + C_L(h). \quad (25)$$

The  $\epsilon_g$  term is nonlinear and will be neglected. The first term is given by,

$$C_L(f_{0e}(p_{\parallel})) = -\tau \nu_e A_{\parallel} f_{0e}, \quad (26)$$

which is implemented as an additional term in the electron weight equation. The third term on the RHS of Eq. 25 is implemented using the Monte-Carlo method. After both the predictor and the corrector step, a random change to the pitch angle variable  $\lambda$  is carried out, with the average amount of change determined by collision frequency and the time step[20,14],

$$\lambda_{\text{new}} = \lambda_{\text{old}}(1 - \nu_e \delta t) \pm \left[ \left( 1 - \lambda_{\text{old}}^2 \right) \nu_e \delta t \right]^{1/2}, \quad (27)$$

where  $\pm$  means equal probability of + or -[20].  $\delta t = \Delta t$  for corrector step and  $\delta t = 2\Delta t$  for predictor step,  $\Delta t$  is the time step of the simulation.

## 4 Simulations

### A. Field-line-following coordinates

In this paper we assume a magnetic equilibrium with circular concentric flux surfaces. The magnetic field strength is  $B(r, \theta) = 1 - (r/R_0) \cos \theta$ . The field-line-following coordinates[15]  $(x, y, z)$  are defined by  $x = r - r_0$ ,  $y = (r_0/q_0)(q\theta - \zeta)$  and  $z = q_0 R_0 \theta$ . Here  $(r, \theta, \zeta)$  are the usual toroidal coordinates,  $R_0$  is the major radius at the magnetic axis,  $r_0$  is the minor radius at the center of the simulation domain,  $q_0 = q(r_0)$  the safety factor. One can think of  $(x, y)$  as labeling the field line and  $z$  as a coordinate along the field line. The particle motion is given by

$$\begin{aligned} \dot{x} &= -\frac{m_\alpha}{q_\alpha B R_0} (v_{\parallel}^2 + v_{\perp}^2/2) \sin \theta - \frac{\partial \langle \phi \rangle}{\partial y} + v_{\parallel} \frac{\partial \langle A_{\parallel} \rangle}{\partial y} \\ \dot{y} &= -\frac{m_\alpha}{q_\alpha B R_0} (v_{\parallel}^2 + v_{\perp}^2/2) (s\theta \sin \theta + \cos \theta) + \frac{\partial \langle \phi \rangle}{\partial x} - v_{\parallel} \frac{\partial \langle A_{\parallel} \rangle}{\partial x} \\ \dot{z} &= v_{\parallel} \frac{R_0}{R}. \end{aligned} \quad (28)$$

Here  $R = R_0 + r \cos \theta$ ,  $s = r_0 q' / q_0$ . The terms dependent on  $\phi$  or  $A_{\parallel}$  in  $\dot{x}$  and  $\dot{y}$  represent nonlinear dynamics due to the  $\mathbf{E} \times \mathbf{B}$  drift and magnetic fluttering.  $\dot{p}_{\parallel}$  in Eq. 2 is found to be

$$\begin{aligned}\dot{p}_{\parallel} = & -\frac{B\mu}{m_{\alpha}} \frac{r}{qR_0^2} \sin \theta - \frac{q_{\alpha}}{m_{\alpha}} \frac{q_0 R_0}{qR} \frac{\partial \langle \phi \rangle}{\partial z} \\ & + \frac{q_{\alpha}}{m_{\alpha}} \left( \dot{x} \frac{\partial \langle A_{\parallel} \rangle}{\partial x} + \dot{y} \frac{\partial \langle A_{\parallel} \rangle}{\partial y} + \dot{z} \frac{\partial \langle A_{\parallel} \rangle}{\partial z} \right) \\ & + \frac{1}{BR_0} \left( v_{\parallel} \frac{\partial \langle \phi \rangle}{\partial x} + \frac{\mu B}{m_{\alpha}} \frac{\partial \langle A_{\parallel} \rangle}{\partial x} \right) \sin \theta \\ & + \frac{1}{BR_0} \left( v_{\parallel} \frac{\partial \langle \phi \rangle}{\partial y} + \frac{\mu B}{m_{\alpha}} \frac{\partial \langle A_{\parallel} \rangle}{\partial y} \right) (\cos \theta + s \theta \sin \theta),\end{aligned}\quad (29)$$

in which the first term on the RHS is the mirror force and is the only term needed for linear simulations. The nonlinear terms account for effects such as trapping and de-trapping of particles due to fluctuations. In this paper we have neglected this parallel nonlinearity.

The simulation domain  $(0, l_x) \times (0, l_y) \times (0, l_z)$  is chosen to be  $l_z = 2\pi q_0 R_0$ , to cover the whole  $\theta$  range.  $l_y$  is typically chosen such that the simulation domain represents a fraction of the full torus, but in principle can be chosen to be  $2\pi r_0 / q_0$ , to cover all toroidal angles. Periodic boundary conditions are used in  $x$  and  $y$ , and toroidal boundary conditions[15] are used in  $z$ . The boundary condition in  $x$  is somewhat arbitrary, as there is no natural way to connect the two radial boundaries based on physical periodicity.

### B. Alfvén and ITG in a shear-less slab

Consider a plasma slab with constant equilibrium magnetic field  $\mathbf{B} = B_0 \hat{\mathbf{z}}$ . Density and temperature are nonuniform in the  $x$  direction. Here we compare the results of linear simulations with the linear dispersion relation discussed in Ref. [8]. The emphasis is to compare simulation results from the new algorithm as presented in Section III with results from the previous algorithm in Ref. [8]. Fig. 1 shows results plotting the Alfvén wave frequency vs.  $\beta_i$ . The plasma is uniform in this case. Results from both the new scheme (triangles) and the old scheme (squares) are shown. The mode wave number is  $k_x \rho_i = 0.2$ ,  $k_y \rho_i = 0.4$  and  $k_{\parallel} \rho_i = 7.14 \times 10^{-4}$ . We choose  $m_i = 1$  hence  $\rho_i = m_i v_{Ti} = 1$ . The box size is given by  $l_x = l_y = 32 \rho_i$ ,  $l_z = 8796 \rho_i$ , number of grids in each dimension is  $N_x = N_y = N_z = 32$ . The split-weight parameter  $\epsilon_g = 0.5$ , electron mass  $m_e = 1/1837$ ,  $\nu_{ei} = 0$ . The time step is  $\Omega_{ci} \Delta t = 1$ , and the number of particles is 1 048 576 per species. The results from the previous scheme show significant deviation from the dispersion relation for  $\beta_i > 0.5\%$ , whereas the results from

the new scheme show very good agreement. Fig. 2 shows similar results for the ITG mode growth rate. The plasma is nonuniform with

$$\kappa_n = -\frac{1}{n_{0\alpha}} \frac{dn_{0\alpha}}{dx} = 0.04, \quad \kappa_{Ti} = -\frac{1}{T_{0i}} \frac{dT_{0i}}{dx} = 0.2, \quad \kappa_{Te} = -\frac{1}{T_{0e}} \frac{dT_{0e}}{dx} = 0.$$

Other parameters are the same as that used in Alfvén wave simulations except that particle number is now 262 144 per species. Results from both the new (triangles) and old (squares) schemes are shown. The new scheme gives accurate results for all  $\beta_i$  values shown, while the old scheme gives less accurate results for low  $\beta_i$  ( $\beta_i/m_e \leq 1$ ) and wrong results for larger  $\beta_i$ .

### *C. Toroidal linear benchmark with Eulerian codes*

Consider a toroidal deuterium plasma ( $m_i = 2$ ) with the Waltz standard case parameter set [21]:  $R_0/a = 3.0$ ,  $r_0/a = 0.5$ ,  $R_0\kappa_{Ti} = R_0\kappa_{Te} = 9.0$ ,  $R_0\kappa_n = 3.0$ ,  $s_0 = r_0 q' / q_0 = 1.0$  and  $q_0 = 2.0$ . Here we compare results of mode growth rate and frequency from the particle code with that from Eulerian codes gks[16] and GYRO[11]. Fig. 3 and Fig. 4 plot the computed data for mode growth rate and frequency as functions of  $\beta_i$ . The mode wave number is  $k_y \rho_i = 0.3$ . The size of the simulation box is  $l_x = 4.71$ ,  $l_y = 29.6$  and  $l_z = 2\pi q_0 R_0$  with  $R_0 = 1000.0$ . The grid numbers are  $8 \times 32 \times 32$ . Time step  $\Delta t = 4$ . A total of 32 768 particles are loaded for each species. The split-weight parameter  $\epsilon_g = 0.5$ . Results from the particle code are converged with respect to  $\epsilon_g$  and  $l_x$ , assuming  $l_x$  is not too big. Results for both the finite- $\beta$  modified ITG branch and the Kinetic Ballooning Mode (KBM) are shown. Given the considerable difference between the two types of codes in methodology, we consider the agreement as reasonable.

### *C. Collisional effects*

Fig. 5 shows the effects of collisions on the linear growth rate of the  $k_y \rho_i = 0.3$  mode at  $\beta_i = 0$ , using previous parameters. Also shown are results from gks and GYRO. To avoid numerical difficulty at small energy  $\varepsilon_e$ , where the collision rate  $\nu_e$  becomes singular, a cut-off velocity  $v_c = 0.05 v_{Te}$  is chosen such that electrons with  $v < v_c$  are not subject to collisions. Growth rates from the particle code at low collision rate is lower than that from the Eulerian codes, possibly caused by different resolution of the velocity space. We have verified that changing the cut-off velocity to  $v_c = 0.1 v_{Te}$  in the particle code causes little change in the results.

#### D. Nonlinear simulations

We use the Cyclone DIII-D Base Case[22] parameters to test the algorithm nonlinearly. These are typical H-mode plasma parameters as follows:  $R/L_{Ti} = 6.9$ ,  $R/L_{Te} = 0$ ,  $R/L_n = 2.2$ ,  $q_0 = 1.4$ ,  $s = 0.78$ ,  $r_0/R = 0.18$ ,  $m_i = 1$ ,  $m_e = 1/1837$ . In the following simulations a collision frequency of  $\nu_{ei}/\omega_{ci} = 3 \times 10^{-4}$  is used. The size of the simulation box is  $l_x \times l_y \times l_z = 65.3\rho_i \times 64\rho_i \times 8796\rho_i$ , grid numbers are  $64 \times 64$ . Time step is  $\omega_{ci}\Delta t = 3$ . A total of 1 048 576 particles is loaded per species. Fig. 5 shows the evolution of the ion heat flux  $\chi_i$  from three runs, with  $\beta_i = 10^{-4}$ ,  $2 \times 10^{-3}$  and with adiabatic electrons ( $\delta n_e = \tau(\phi - \langle \phi \rangle)$  with  $\langle \phi \rangle$  being the average  $\phi$  on a flux surface). The estimated steady state diffusivity for the adiabatic electron run is approximately  $\chi_i L_n / \rho_i^2 v_{Ti} \approx 2.3$ , in agreement with other gyrokinetic particle codes[22]. The inclusion of kinetic electrons (both trapped and passing) at  $\beta_i = 10^{-4}$  increases the maximum growth rate from  $\gamma L_n / v_{Ti} = 0.11$  to  $\gamma L_n / v_{Ti} = 0.16$  and increases  $\chi_i$  roughly in proportion. Increasing beta to  $\beta_i = 0.002$  (corresponding to total plasma beta of  $\beta = 0.8\%$ ) reduces the maximum growth rate to  $\gamma L_n / v_{Ti} = 0.07$  and the steady state diffusivity to  $\chi_i L_n / \rho_i^2 v_{Ti} \approx 0.7$ , well below the adiabatic electron level. Much larger ion heat fluxes are observed as  $\beta_i$  is increased to above the KBM threshold. The experimentally measured ion heat diffusivity for the DIII-D shot (shot #81499 at time t=4000ms, for which the base case parameters are based on) is  $\chi_i L_n / \rho_i^2 v_{Ti} \approx 0.16$  [22], much lower than the adiabatic electron level. Although a direct simulation of the experiment is not attempted here, as we do not yet have effects such as profile variation, realistic geometry, impurities, etc., in the model, the simulation results indicate that electromagnetic effects on the ITG turbulence play an important role in determining the transport level.

## 5 Conclusion

In this paper we have developed an algorithm for the simulation of microin-stabilities on the space scale of the ion Larmor radius with kinetic electrons and electromagnetic perturbations, keeping  $\delta B_\perp$  and neglecting  $\delta B_\parallel$ . Keeping only perpendicular magnetic field perturbations is valid for low beta plasmas. The key elements of the algorithm comprise of: 1) an adjustable split-weight scheme that allows for an increase in the time step to a practically acceptable level in nonlinear simulations of multiple modes; and 2) an algorithm for solving Ampere's equation for moderate  $\beta$ ,  $\beta_i m_i / m_e \gg 1$ , in which the current carried by the zero-order distribution is evaluated using the marker particle population in such a way as to ensure accurate cancellation with the corresponding current carried in  $\delta f$ . The algorithm was thoroughly tested linearly in shear-less slab geometry where analytical dispersion relation is available.

Linear comparisons with the gks and GYRO toroidal continuum codes are also good. Finally, nonlinear simulations in toroidal geometry show that the ion energy flux decreases as  $\beta$  is increased, but with  $\beta$  still below the kinetic ballooning limit. Above the kinetic ballooning threshold, the simulations show energy fluxes that are ten or more times higher than corresponding electrostatic simulations.

## Acknowledgement

We thank Drs. W. Dorland, J. Candy and R. Waltz for help with benchmarking with gks and GYRO and useful discussions. We are grateful for support from the U.S. Department of Energy, Office of Fusion Energy Sciences. Work is part of the DOE Scientific Discovery through Advanced Computing, Plasma Microturbulence Project.

## References

- [1] S. Parker, W. Lee, R. Santoro, Phys. Rev. Lett. 71 (1993) 2042.
- [2] A. Dimits, T. Williams, J. Byers, B. Cohen, Phys. Rev. Lett. 77 (1996) 71.
- [3] R. Sydora, V. Decyk, J. Dawson, Plasma Phys. Controlled Fusion 38 (1996) A281.
- [4] Z. Lin, T. Hahm, W. Lee, W. Tang, R. White, Science 281 (1998) 1835.
- [5] J. Cummings, Ph.D. thesis, Plasma Physics Lab, Princeton University (1994).
- [6] B. Cohen, A. Dimits, J. Stimson, D. Barnes, Implicit-moment partially linearized particle simulation of kinetic plasma phenomena, LLNL Report UCRL-JC-121734, September 1995 .
- [7] I. Manuilskiy, W. W. Lee, The split-weight particle simulation scheme for plasmas, Phys. Plasmas 7 (2000) 1381.
- [8] Y. Chen, S. E. Parker, Gyrokinetic turbulence simulations with kinetic electrons, Phys. Plasmas 8 (2001) 2095.
- [9] T. S. Hahm, W. W. Lee, A. Brizard, Nonlinear gyrokinetic theory for finite-beta plasma, Phys. Fluids 31 (1988) 1940.
- [10] F. Jenko, Comp. Phys. Comm. 125 (2000) 196.
- [11] J. Candy, R. Waltz, An eulerian gyrokinetic-maxwell solver, General Atomics Report GA-A23876.

- [12] W. W. Lee, J. L. V. Lewandowski, T. S. Hahm, Z. Lin, Shear-alfvn waves in gyrokinetic plasmas, *Phys. Plasmas* 8 (2001) 4435.
- [13] M. Kotschenreuther, *Bull. Am. Phys. Soc.* 34 (1988) 2107.
- [14] Y. Chen, R. B. White, Collisional  $\delta f$  method, *Phys. Plasmas* 10 (1997) 3591.
- [15] M. A. Beer, S. C. Cowley, G. W. Hammett, Field-aligned coordinates for nonlinear simulations of tokamak turbulence, *Phys. Plasmas* 2 (1995) 2687.
- [16] M. Kotschenreuther, G. Rewoldt, W. Tang, *Comp. Phys. Comm.* 88 (1995) 128.
- [17] W. Dorland, Proc. 18th Intnl. Conf. on Fusion Energy, Internal Atomic Energy Agency, Sorrento, Italy, 2000 .
- [18] W. W. Lee, Gyrokinetic approach in particle simulation, *Phys. Fluids* 26 (1983) 556.
- [19] W. Lee, Gyrokinetic particle simulation model, *J. Comput. Phys.* 72 (1987) 243.
- [20] A. H. Boozer, G. Kuo-Petravic, Monte carlo evaluation of thansport coefficients, *Phys. Fluids* 24 (1981) 851.
- [21] R. E. Waltz, G. Kerbel, J. Milovich, Toroidal gyro-landau fluid model turbulence simulations in a nonlinear ballooning mode representation with radial modes, *Phys. Plasmas* 1 (1994) 2229.
- [22] A. Dimits, et al., Comparisons and physics basis of tokamak transport models and turbulence simulations, *Phys. Plasmas* 7 (2000) 969.

## **Fifure Captions**

Fig. 1 Alfvén wave frequency vs.  $\beta_i$ . Solid line is from the dispersion relation. Data points shown in squares are from the old algorithm [8], points in triangles are from the new algorithm.

Fig. 2 Growth rate of the ITG mode vs.  $\beta_i$ .

Fig. 3 Growth rate of the  $k_y \rho_i = 0.3$  mode vs.  $\beta_i$  for the Waltz standard case. Solid line is from GYRO, dashed line from **gks**, points from the particle code.

Fig. 4 Frequency of the  $k_y \rho_i = 0.3$  mode vs.  $\beta_i$  for the Waltz standard case.

Fig. 5 Growth rate the  $k_y \rho_i = 0.3$  mode vs.  $\nu_e i$  for the Waltz standard case.

Fig. 6 Evolution of the ion heat diffusivity in time.

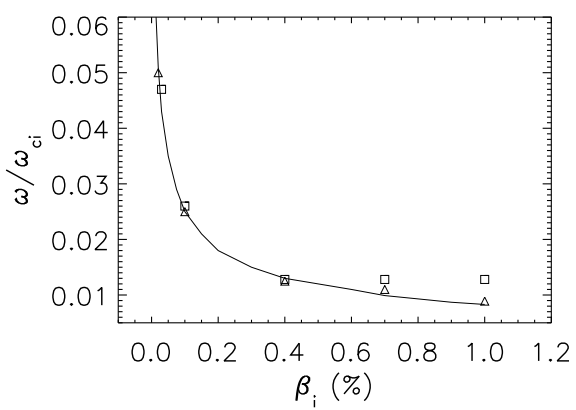


Fig. 1.

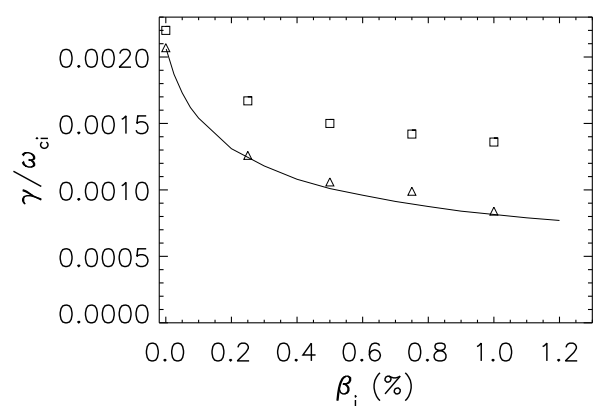


Fig. 2.

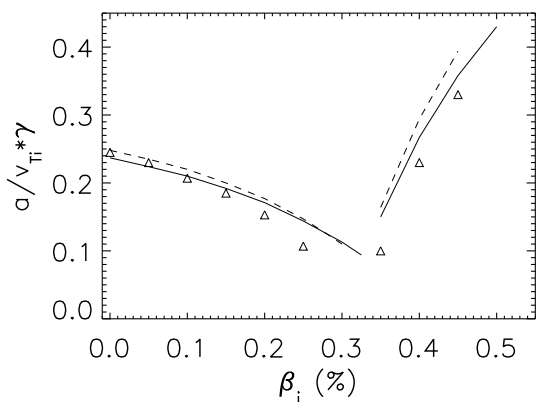


Fig. 3.

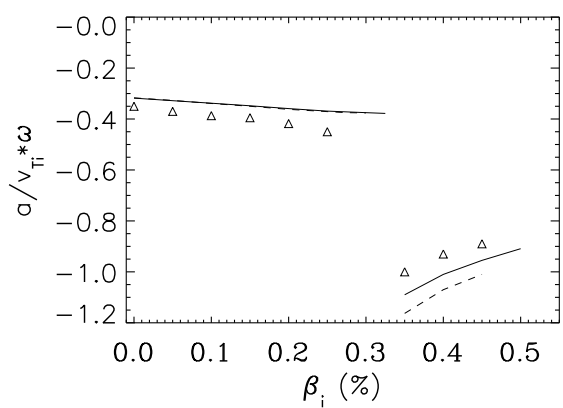


Fig. 4.

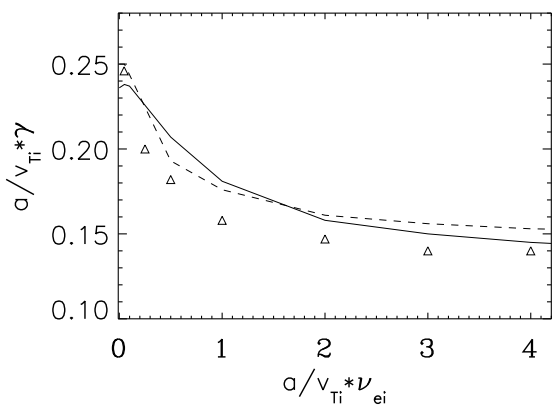


Fig. 5.

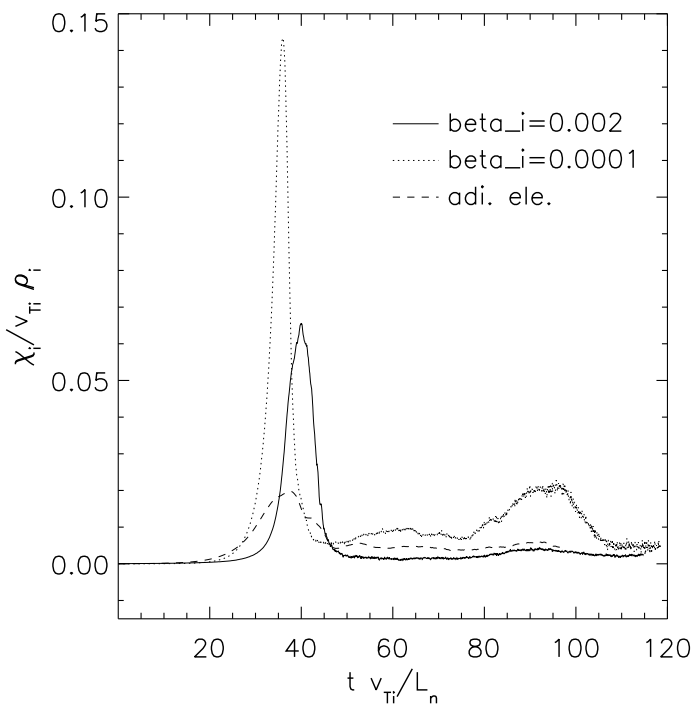


Fig. 6.